Bragg scattering based acoustic topological transition controlled by local resonance

Taehwa Lee* and Hideo Iizuka
Toyota Research Institute of North America, Toyota Motor North America, Ann Arbor, Michigan 48105, USA

(Received 27 November 2018; revised manuscript received 25 January 2019; published 27 February 2019)

Topological metamaterials offer new routes for control of waves, which are widely realized by Bragg scattering and/or local resonance. Understanding of topological transition by the interaction between these mechanisms is strongly desired to extend the design degrees of freedom for intriguing wave phenomena. Here, we demonstrate a phononic metamaterial consisting of C-shaped elements that enables us to investigate interaction between Bragg scattering and local resonance. We show that by adding resonance scattering a topological band gap is opened from a Bragg scattering based Dirac cone, and its band gap is controlled by the resonance frequency of the cavities relative to the Dirac cone frequency. In addition, we show that topological band-gap opening induced by the Bragg scattering can be reversed into an ordinary state or vice versa by judicious inclusion of the local resonance. Scattering cross-section analysis elaborates the combined effect of the two mechanisms on topological states. By employing lossy resonant elements, we further demonstrate a lossy topological insulator capable of one-way sound propagation immune to sharp corners, potentially leading to an energy-harvesting topological insulator. Our results provide a critical understanding of topological phenomena involving coupled scattering mechanisms.

DOI: 10.1103/PhysRevB.99.064305

I. INTRODUCTION

Topological insulators have drawn much attention, since their topological invariant enables robust one-way wave propagation immune to perturbations such as defects and disorders [1–3]. After the first demonstration of the acoustic version of topological insulators using rotating flows [4,5], flow-free acoustic topological insulators were quickly introduced by realizing pseudospin states [6–8]. Since then, there have been extensive research efforts devoted to seeking different types of topological phononic crystals [9–19]. In these works, a topological phase transition was enabled by carefully controlling symmetry breaking in two-dimensional (2D) phononic crystals. Beyond the 2D topological insulators, the research on topological acoustics has evolved into higher-order topological insulators (quadrupolar) [20] and other dimensionalities, e.g., three-dimensional (3D) [21] and one-dimensional [22,23]. In addition, to prove its practical merits, backscattering-free edge propagation has been combined with additional intriguing functionalities such as acoustic antenna [24], programmable coding [25], bilayer [26], multiband [27], acoustic delay line [28,29], tunable strain [30,31], and on-chip [32].

Similar to conventional phononic crystals, the scattering mechanisms employed in these acoustic topological insulators include Bragg scattering and local resonance. Bragg scattering has been commonly used in acoustic topological insulators, since it requires a simple design process. In addition, local resonance has shown advantages by enabling subwavelength control of waves [33–35]. An interesting feature in topological insulators may be demonstrated by implementing other scattering mechanisms (e.g., inertial amplification [36]), or by simultaneously using more than two mechanisms. Especially, combination of these mechanisms is advantageous in increasing the degrees of freedom as a synthetic dimension necessary for higher-order topological modes (beyond the octupole moment) [37]. In a system with combined mechanisms, interaction between the constituent scattering mechanisms is important, requiring a platform that allows multiple mechanisms. Recently, it has been demonstrated that one platform can encompass three scattering mechanisms by engineering spiral scatterers [13]. However, in this system, each mechanism was independently employed. There have been no systematic studies on interaction between the scattering mechanisms in acoustic topological insulators, as previous works are focused on one of the scattering mechanisms [9–19].

In this paper, we study interaction between the Bragg scattering and local resonance. To independently control the effect of each mechanism in phononic crystals, we use C-shaped elements that are constructed by circular rods with inside circular cavities and narrow slits. We find that the local resonance induced by the inner cavities and slits leads to band-gap opening and the topological phase transition in Bragg scattering. The size of the band-gap opening is strongly influenced by the resonance frequency relative to the frequency where the double Dirac cone appears. In addition, topological states are determined by the orientation of the slits as well as the resonance frequency. By employing scattering cross-section analysis, we investigate the effect of the resonance on the Bragg scattering induced topological phase transitions. Lastly, we show that the lossy topological insulator, which is constructed by including losses into the resonant elements, exhibits robust one-way transmission.

*taehwa.lee@toyota.com

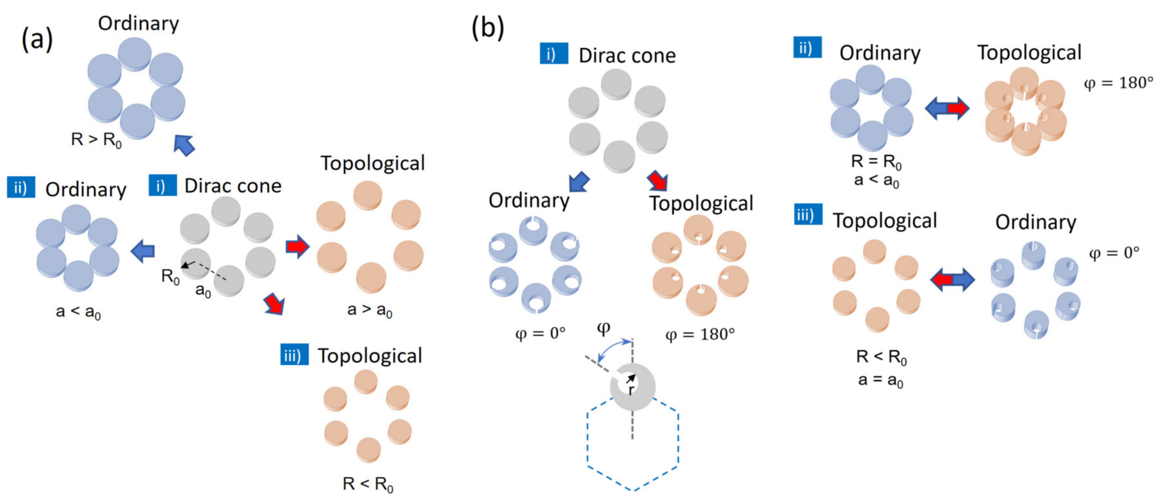

FIG. 1. (a) Conventional topological phase transitions with respect to the double Dirac cone for $R/a = R_0/a_0 = 0.3928$ with the lattice constant, a, and the radius, R. The topological transitions occur via the change of the hexagon (varying a for the constant $R = R_0$) or different radii (R) for the constant $a = a_0$. (b) Resonant cavity-induced Bragg scattering topological phase transitions, depending on the slit orientation (φ) and the cavity radius (r) of the resonant element: (i) from the Dirac cone ($R = R_0$, $a = a_0$) to the ordinary ($\varphi = 0^\circ$) or topological ($\varphi = 180^\circ$) state, (ii) from the ordinary ($R = R_0$, $a < a_0$) to topological state ($\varphi = 180^\circ$), and (iii) from the topological ($R < R_0$, $a = a_0$) to ordinary state ($\varphi = 0^\circ$).

II. DESIGN OF THE C-SHAPED SCATTERER

To study interaction of local resonance with Bragg scattering, we first consider a honeycomb lattice consisting of circular rods (the radius R and the lattice constant a) in air, which features a Bragg scattering induced double Dirac cone with a fourfold degeneracy for $R/a = 0.3928$. Such a double Dirac cone occurs as a feature of phononic crystals characterized by C_{6v} point-group symmetry. We have chosen a honeycomb lattice widely implemented for topological insulators, although a triangular lattice of ring-type scatterers can show the double Dirac cone [9]. The double Dirac cone with four degenerate modes creates pseudo-spin-up and -down states by hybridizing these modes. The specific R/a for the double Dirac cone is obtained from simulation (see Appendix A) using a hard boundary condition on the scatterers (the same R/a for the double Dirac cone was reported for steel rods and air in Ref. [7]). Owing to a symmetry inversion in the reciprocal space, this phononic crystal results in energy-band inversion and thereby topological phase transition from an ordinary state to a topological state. Here, the ordinary state (i.e., a topologically trivial state) is characterized by two dipolar modes in the lower-frequency bands and two quadrupolar modes in the upper-frequency bands (i.e., zero-spin Chern number), whereas the topological state is characterized by two quadrupolar modes in the lower bands and two dipolar modes in the upper bands (non-zero-spin Chern number). As summarized in Fig. 1(a), it is well known that the topological phase transition is readily realized by either controlling the filling ratio (R/a) [7] or changing the size of the hexagon (expanded or shrunk) [38]. Then, we add local resonance into the non-resonant crystals by integrating resonant elements consisting of a cavity and a narrow slit, as shown in Fig. 1(b). For the C-shaped elements, the cavity (area S) and slit (width h and length l_s) constitute a Helmholtz resonator, the resonance frequency (f_r) of which is approximately given by $f_r = \frac{c}{2\pi}\sqrt{\frac{h}{Sl_s}}$.

For independent control of each contribution of local resonance and Bragg scattering, we assume that these resonant elements only result in additional scattering without changing the Bragg scattering owing to the negligible rigidity change and the small slit width ($h \ll \lambda$, wavelength). In Fig. 1(b), we show that adding the resonant elements to the gapless phononic crystal [case i in the figure, the double Dirac cone] leads to band-gap openings (two twofold degeneracies) with an ordinary or topology state depending on the radius of the cavity and the orientation of the slit (defined as φ): the ordinary ($\varphi = 0^\circ$) and topological ($\varphi = 180^\circ$) states. For the orientations ($\varphi = 0^\circ$ and 180°) of the resonant elements, C_{6v} point-group symmetry is preserved. Moreover, the resonance can change topological states in phononic crystals with bulk band gaps: the high-filling ratio crystal [case ii in the figure] from an ordinary to a topological state by resonance ($\varphi = 180^\circ$), and the expanded crystal [case iii in the figure] from a topological to an ordinary state by $\varphi = 0^\circ$.

III. RESULTS AND DISCUSSIONS

A. Topological phase transition in C-shaped phononic crystals

Figure 2(a) shows the band structures of the phononic crystals [case i in Fig. 1(b)]. The phononic crystal with no resonant elements ($R =$ 15 mm, $a =$ 38.2 mm, and $R/a = 0.3928$) leads to the double Dirac cone at a frequency of $f_D = 5100$ Hz, where four conical bands touch at a point. We find that reduced Dirac cone frequency ($f_D a$) in this paper is the same as that used in Ref. [7], i.e., $f_D a = 193.8$ m/s, indicating that the Dirac cone frequency for different a can be estimated by $f_D = 193.8$ (m/s)$/a$ if a hard boundary condition is imposed on scatterers in air. The addition of circular cavities with different radii and orientations (radius $r = 6$ mm, $\varphi = 0^\circ$; $r = 4$ mm, $\varphi = 180^\circ$), respectively, results in ordinary and topological states having similar band-gap sizes (~400 Hz).

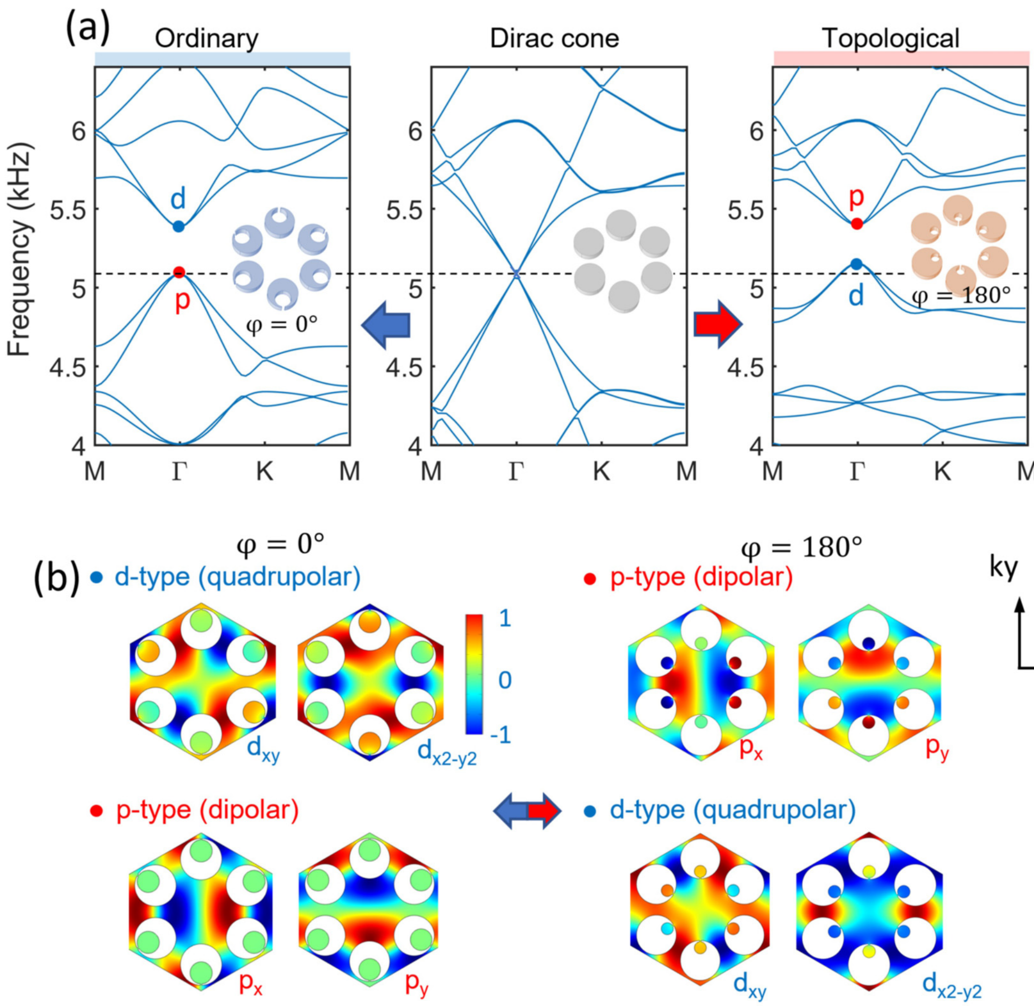

FIG. 2. (a) Band structures of the honeycomb phononic crystals for the ordinary state (left), double Dirac cone (middle), and topological state (right). For the ordinary state, the radius (r) and orientation (φ) are given by $r = 6$ mm and $\varphi = 0^\circ$, while for the topological state $r = 4$ mm and $\varphi = 180^\circ$. The topological band inversion occurs (d type, quadrupolar; p type, dipolar). The horizontal dashed line indicates the frequency (f_D) at which the double Dirac cone occurs. (b) Pressure fields for the ordinary (left panel) and topological (right panel) states. The d-type (quadrupolar) bulk modes correspond to d_{xy} and d_{x2-y2}, while the p-type (dipolar) bulk modes correspond to p_x and p_y [$p_x : x_-/y_+$, $p_y : x_+/y_-$, $d_{x2-y2} : x_+/y_+$, and $d_{xy} : x_-/y_-$ with $x(y)_\pm$ the even or odd symmetry along the x or y axis].

The topological state is confirmed with the band inversion, showing d-type (quadrupolar) bands at lower frequencies and p-type (dipolar) bands at higher frequencies (± 1 Chern numbers), whereas the ordinary state exhibits lower p-type bands and upper d-type bands (zero Chern number). The circular cavities along with the identical slit size ($h = l_s = 1$ mm) have resonance frequencies of 2000 Hz ($r = 6$ mm) and 4200 Hz ($r = 4$ mm), much smaller than the frequency ($f_D = 5100$ Hz). This indicates that these resonant elements serve as off-resonance scatterers, but they significantly influence topological phases. One interesting feature is that such local resonance dominantly affects only either of the two band types while the other band type remains similar in its corresponding frequency at Γ (close to $f_D = 5100$ Hz). Specifically, for the ordinary state, the frequencies of the quadrupolar states (d type) are only increased by the local resonance, whereas for the topological states only the dipolar states (p type) considerably experience their frequency shifts. Such orientation dependence of the topological phases is explained by the pressure field inside the cavities, as shown in Fig. 2(b). Here, the subscripts of p and d represent the symmetry of the pressure field [$p_x : x_-/y_+$, $p_y : x_+/y_-$, $d_{x2-y2} : x_+/y_+$, and $d_{xy} : x_-/y_-$ with $x(y)_\pm$ the even or odd symmetry along the x or y axis]. For the ordinary state ($\varphi = 0^\circ$), the dipolar field profiles are negligibly influenced by the resonant elements, showing low pressures in the cavities (green). Notably, the slits of the cavities are aligned to the nodal line of the pressure field. In contrast, the quadrupolar states have relatively high pressure in the cavities away from the nodal lines. We find that the topological states ($\varphi = 180^\circ$) show strong coupling of the cavities with the dipolar pressure fields, thus causing the dipolar (p-type) bands to blueshift.

For much stronger interaction between local resonance and Bragg scattering, it is natural to consider the resonance frequency (f_r) close to f_D. To control the resonance frequency, we vary the radius (r) of the resonant cavity in the phononic

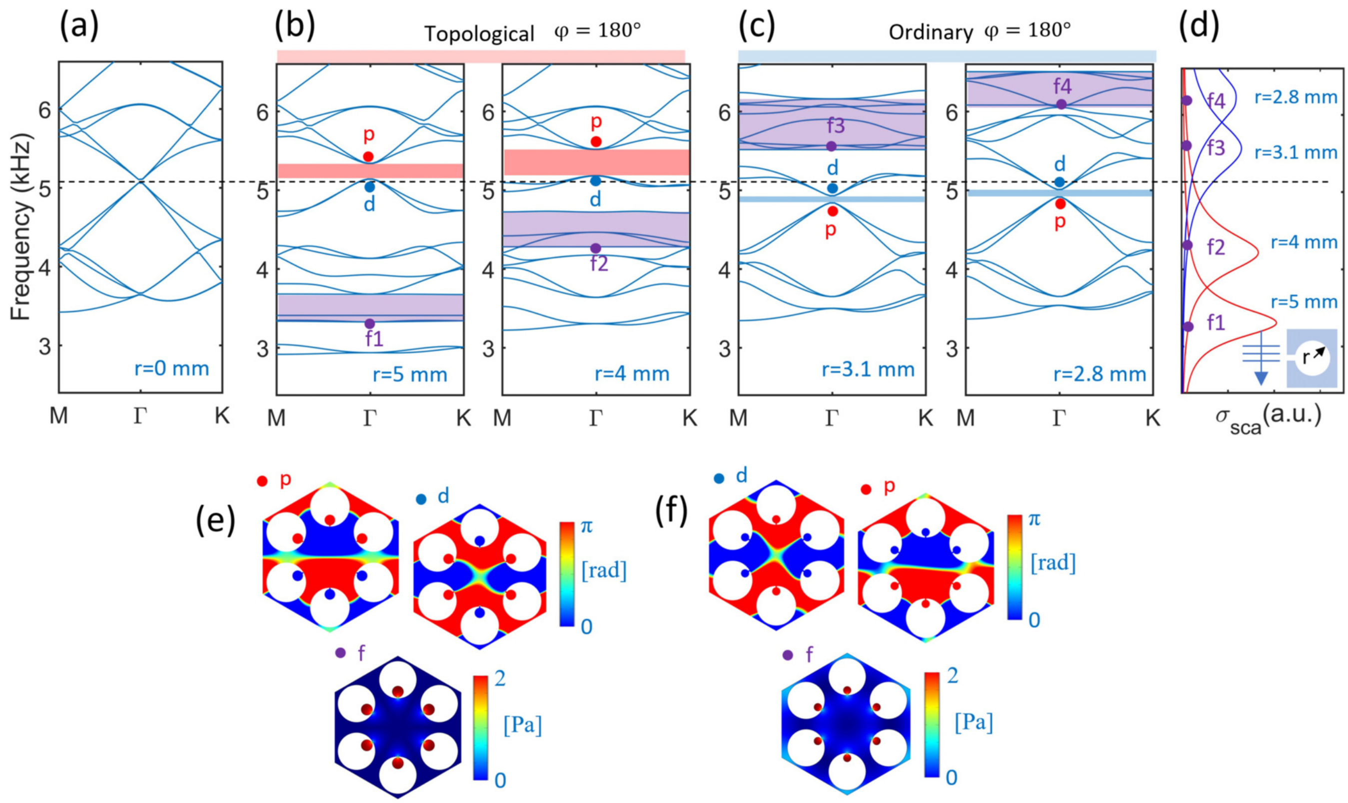

FIG. 3. Interaction between Bragg scattering and local resonance with varying the radius (r) of the circular cavity. (a) Band structure for the crystal with no resonance ($r = 0$ mm and $R = 15$ mm), showing the double Dirac cone. (b) Topological band structures of the phononic crystals ($\varphi = 180^\circ$) for $r = 5$ mm and $r = 4$ mm, the resonance frequencies (f_r) of which are smaller than the Dirac cone frequency (f_D), i.e., $f_r < f_D$. The red shade and purple shade indicate band gaps and resonance-induced flat bands, respectively. The dipolar (quadrupolar) bands are indicated as p with red circle symbols (d with blue circle symbols) at the Γ point. The frequency of the lower flat band, labeled as f with purple circle symbols, corresponds to the resonance frequency. (c) Ordinary band structures of the phononic crystals ($\varphi = 180^\circ$) for $r = 3.1$ and 2.8 mm ($f_r > f_D$). (d) Simulated scattering cross section of isolated resonant scatterers, illustrated in the inset. (e, f) Phase plots (top two, p_y and d_{x2-y2}) and acoustic intensity field (bottom, f at resonance) of the topological ($r = 4$ mm) (e) and ordinary ($r = 3.1$ mm) (f) states.

crystals of $\varphi = 180^\circ$ [Fig. 2(a)] while the slit size remains the same. The scattering cross-section spectra for different r in Fig. 3(d) show that the resonance frequency increases with reducing r. Starting from the band structure for $r = 0$ mm showing the double Dirac cone [Fig. 3(a)], we observe an increase in the topological band gap from 200 to 400 Hz by reducing r ($5 \rightarrow 4$ mm) and thereby the frequency difference ($f_D - f_r$), as shown in Fig. 3(b). In the band structure, such a resonance-frequency shift is also confirmed with resonance-created bands, which are highlighted as the purple shade. It is interesting to note that the local resonance significantly influences the topological phase transition despite its small scattering cross section at frequencies around f_D. Note that although the scattering analysis of an isolated resonant scatterer provides an insight into understanding of the topological phase transitions its scattering characteristics are different from those of an array of resonant scatterers (each strongly coupled with the others).

When the cavity radius (r) is further reduced, the resonance frequency (f_r) is increased, exceeding f_D, i.e., $f_r > f_D$, as shown in Figs. 3(c) and 3(d). In Fig. 3(c), we find that the band gaps for $r =$ 3.1 and 2.8 mm are relatively small (~50 Hz) compared to those for $f_r < f_D$. Interestingly, for $f_r > f_D$ we observe band inversion into the ordinary state (i.e., d-type bands at higher frequencies). This feature is explained with the pressure phase of the cavities, as shown in Figs. 3(e) and 3(f). Depending on sign ($f_r - f_D$), the phase polarity of the resonant cavity is drastically changed. For the topological crystals ($f_r < f_D$), the polarity of the inner cavities is out of phase in the dipolar field [Fig. 3(e)], whereas for the ordinary crystal ($f_r > f_D$) the polarity in the dipolar field is reversed to be in phase [Fig. 3(f)]. This indicates that the polarity of the cavity determines the effect of the resonance scattering on the topological phase transition.

The topological transition depending on sign ($f_r - f_D$) for $\varphi = 180^\circ$ is similarly observed for $\varphi = 0^\circ$. Figures 4(b) and 4(c) summarize the frequencies of p- and d-type bands at Γ with respect to the cavity radius (r) for the phononic crystals of $\varphi = 0^\circ$ and 180°, respectively. The resonance frequency for different r is shown in Fig. 4(a). For both $\varphi = 0^\circ$ and 180°, the band gaps are similarly increased by decreasing r down to 4 mm, i.e., increasing the resonance frequency. Moreover, it is noted that for the same r the band gaps of $\varphi = 0^\circ$ are much larger than those of $\varphi = 180^\circ$. Such a difference in the band-gap size between the orientations arises from the coupling between the resonators that depends on the orientation. For $r = 3.5$ mm, the resonance frequency is similar to f_D, i.e., $f_r \approx f_D$. In this case, the local resonance

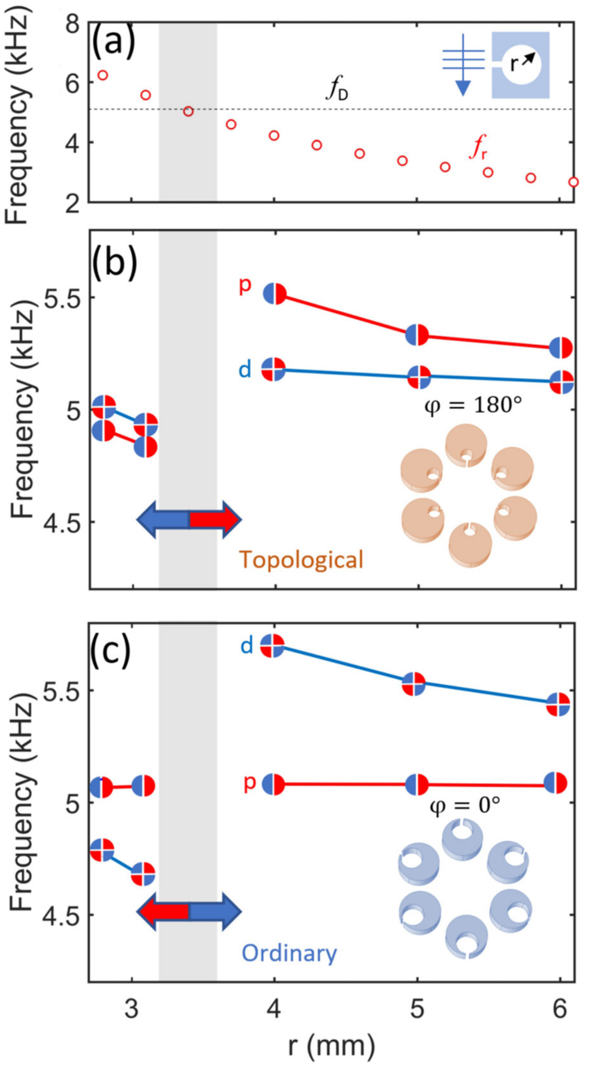

FIG. 4. Band-gap size and topological phase transition. (a) Resonance frequency (f_r) with respect to the radius (r) of the circular resonant cavity. The horizontal dashed line indicates the frequency (f_D) for the double Dirac cone of the nonresonant phononic crystal ($r = 0$). The gray shade region indicates that the radii lead to $f_r \cong f_D$. (b, c) Band-gap sizes as a function of r for the two phononic crystals, $\varphi = 0^\circ$ (b) and $\varphi = 180^\circ$ (c). p-type (red line) and d-type (blue line) bands are labeled as p and d.

appears within the band gap induced by the Bragg scattering (see Appendix B).

B. Scattering cross-section analysis

As the topological phase transition is induced by the interaction between the local resonance and Bragg scattering, we investigate such interaction from a scattering cross-section perspective. Although the band structures of our phononic crystals are determined by scattering from an ensemble of the C-shaped scatterers, the scattering cross-section analysis of an individual scatterer is useful because it allows us to identify the contribution of each scattering mechanism. To see each one's contribution, the C-shaped scatterer is decomposed into the direct and resonant components, as illustrated in Fig. 5(a). The direct component (i.e., geometrical scattering) corresponds to a rigid rod, while the resonant component is modeled as a resonant cavity embedded in a semi-infinite reflector. Such decomposition is valid for the slit widths much smaller than both the wavelength and the outer radius ((R). Such subwavelength slits do not lead to scattering from the direct pathway (i.e., geometrical scattering), but they affect resonant scattering. For the resonant component, the incident wave is parallel to the semi-infinite reflector to prevent the direct scattering by the reflector. In contrast, the circular surface of the C-shaped scatterer dominantly contributes to the direct scattering and the effect of the slits on the direct scattering is negligible, because the slit width is much smaller than the outer radius (R) of the scatterer. Thus, the direct scattering from the C-shaped scatterer can be modeled by using a solid rod. To construct an analytical model, the scattered pressure field by an isolated C-shaped scatterer is expressed by the sum of the direct and resonant scatterings:

$$p_{\mathrm{sc}} = p_{\mathrm{sc,\ dir}} + p_{\mathrm{sc,res}}. \tag{1}$$

For the small slit width ($l_s \ll \lambda$), the directly scattered field is identical to the scattered field by the solid cylinder, which at a point (r, θ) is given by [39]

$$p_{\mathrm{sc,dir}}(r, \theta) = \sum_{n=-\infty}^{\infty} A_n H_n^{(1)}(kr) e^{in\theta}, \tag{2}$$

where $H_n^{(1)}$ is the Hankel function of the first kind, k is the wave number, and $A_n = -e^{in\pi/2}\frac{J_n'(kR)}{H_n^{(1)\prime}(kR)}$ is given for the Neumann boundary condition on the cylinder's surface with the prime being the derivative. The pressure by the resonance is expressed with uniform velocity (v_0) over the slit width by [40]

$$p_{\mathrm{sc,res}}(r, \theta) = -\frac{i\omega\rho h}{4\pi R} v_0\, G(r, R, \theta, \theta_0), \tag{3}$$

where $G(r, R, \theta, \theta_0)$ is the Green's function of a cylinder in a free field, given by $G(r, R, \theta, \theta_0) = -\frac{2}{kR}\sum_{n=-\infty}^{\infty}\frac{H_n^{(1)}(kr)}{H_n^{(1)\prime}(kR)}e^{in(\theta-\theta_0)}$.

The scattering cross section of a scatterer is defined as the ratio of the scattered power to the incident power. The scattered power is calculated by integration of Eq. (1) taken over the spherical surface surrounding the scatterer (see Appendix C for details). Figure 5(a) shows calculated scattering cross sections, which are normalized to the scattering cross-section limit of a subwavelength resonant scatterer, i.e., $\sigma_0 = 2\lambda_0/\pi$ (λ_0 being the wavelength at resonance frequency). The numerical results (symbols) show good agreement with the analytical results (solid line) obtained from Eqs. (2) and (3). We find that the scattering cross section of the resonant component (blue square) around the resonance is comparable to that of the direct component (black triangle). The sum (dashed line) of scattering cross sections of direct (black triangle) and resonant (blue square) components differs greatly from that of the C-shape scatterer (red circle). For frequencies higher than f_r, the scattering cross section of the C-shaped scatterer is decreased due to the destructive interference, whereas for $f < f_r$ it is constructively increased.

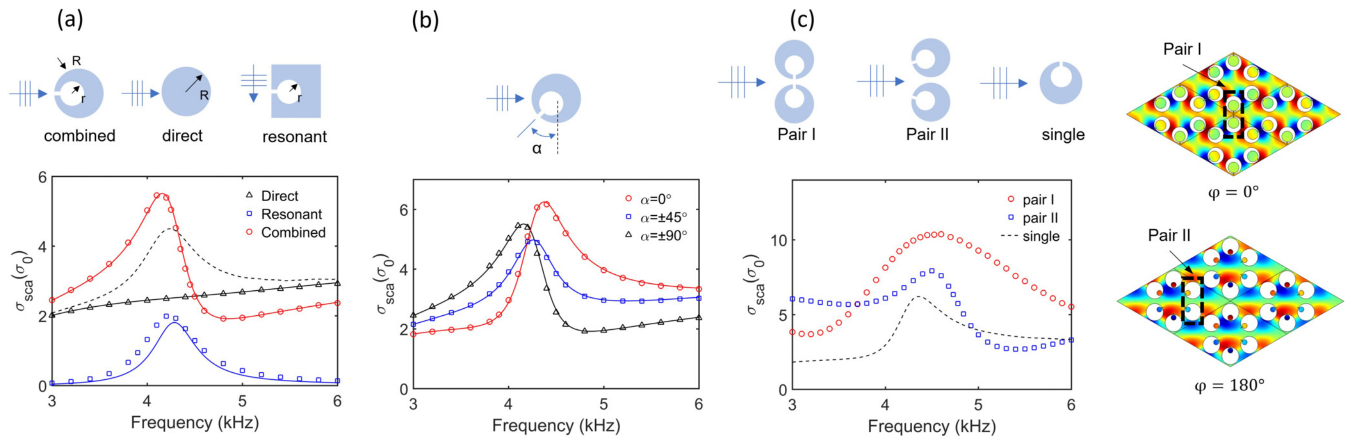

FIG. 5. (a) Scattering cross sections of isolated scatterers: C-shaped rod (combined), solid rod (direct), and resonant cavity (resonant). The dimensions are given by $r = 4$ mm, $R = 15$ mm, and $h = l_s = 1$ mm. For the C-shaped scatterer, the orientation of its slit is aligned to the direction of the incident wave, whereas for the resonant cavity the slit orientation is perpendicular to the incident wave. The scattering cross section is normalized to $\sigma_0 = 2\lambda_0/\pi$. The dashed line corresponds to the sum of the scattering cross sections of the solid rod and resonant cavity. The symbols indicate numerical results (COMSOL Multiphysics), while the solid lines represent analytical results obtained from Eqs. (2) and (3). (b) Angular dependence of the scattering cross section for the C-shaped rods (the angle α is defined as the angle between the slit orientation and the line vertical to the incident wave): $\alpha = 0^\circ$, $\pm 45^\circ$, and $\pm 90^\circ$. The symbols indicate numerical results, while the solid lines represent analytical results. (c) Scattering cross section of the pairs of the C-shaped rods with different slit orientations: two slits facing each other (pair I) and with an angle of 60° (pair II). Pair I constitutes the phononic crystal of $\varphi = 0^\circ$, while pair II is for $\varphi = 180^\circ$. For comparison, the scattering cross section of the single C-shaped rod is plotted (black dashed line).

Such interference asymmetrical to f_r provides an explanation of the sign$(f_r - f_D)$ dependence of the topological phase transition, observed in Figs. 3 and 4.

For the isolated scatterers, the result in Fig. 5(a) is limited to the specific angle of incidence with respect to the orientation of the slit. For the phononic crystals, the slits of the C-shaped scatterers within the unit cell have different angles with respect to the incident wave, thus affecting the scattering cross section. The angular dependence of the scattering cross section is shown in Fig. 5(b). The scattering cross-section spectra are identical between angles of $\alpha = +\alpha_0$ and $-\alpha_0$. With decreasing $|\alpha|$, the scattering cross section decreases for $f < f_r$, while it increases for $f > f_r$. Note that for $\alpha = 0^\circ$ the opposite trend of the spectral characteristic is observed, compared to $\alpha = \pm 90^\circ$.

The quality (Q) factor of the resonators is an important parameter to characterize the interaction of local resonance with the Bragg scattering. It is known that the resonance Q factor is strongly influenced by radiation impedance [40] and thereby coupling of resonators. Thus, to study coupling of the C-shaped resonators, we consider two representative resonator pairs, each from the two phononic crystals ($\varphi = 0^\circ$ and 180° with the same size resonant elements), as illustrated in Fig. 5(c). For the C-shaped resonator pair from the crystal of $\varphi = 0^\circ$ (pair I), the slits of the resonator face each other, while the other resonator pair (pair II) has an angle of 60° between the orientations of the two slits. In Fig. 5(c), the scattering cross section of the coupled resonators (pairs I and II) shows a broader bandwidth than the single resonator, having a lower Q factor. This broadened spectrum by the coupled resonance can explain why the off-resonance scatterers can effectively interact with the Bragg scattering [see the band-gap opening by $f_D - f_r \sim 3000$ Hz in Fig. 3(b)]. Note that pair I has slightly larger scattering cross section than pair II because of its short distance and thereby strong coupling. Such a difference between pair I and pair II provides an explanation for the band-gap size difference between $\varphi = 0^\circ$ and 180° [Figs. 4(b) and 4(c)]. This indicates that although the characteristics of the phononic crystals are fully analyzed by the ensemble of the constituent scatterers the scattering cross-section analysis of a few scatterers is useful in understanding the observed topological phase transitions by local resonance and Bragg scattering.

C. Lossy topological edge mode

We show robust one-way edge propagation at the boundary between different topological states. To investigate these edge modes, we use two different phononic crystals in the inset of Fig. 2(a). The band gaps of these two crystals are similar in size, as shown in Fig. 2(a). The dispersion of interface modes in a supercell composed of these crystals [Fig. 6(a)] is calculated from simulation (see Appendix A), as in Fig. 6(b). We obtain two band-gap-crossing edge modes because of the moderate band-gap size (larger band gap leads to gapped edge states [34]). Also plotted are the pressure fields around the interface between the ordinary and topological states at a frequency of 5200 Hz and wave vectors of $\pm 0.075\pi/a$, and the red arrows indicate the acoustic intensity vectors (i.e., Poynting vectors). We observe the rotational vector fields resulting from modal hybridization [10], mimicking spin-up and spin-down states.

Topological invariants are manifested in immunity to defects and disorders, supporting loss-free one-way sound propagation. As in reality loss is sometimes unavoidable, a critical question that arises is whether topological edge modes are preserved in systems with non-negligible loss [41,22]. Our C shape is an ideal platform to investigate loss effects on

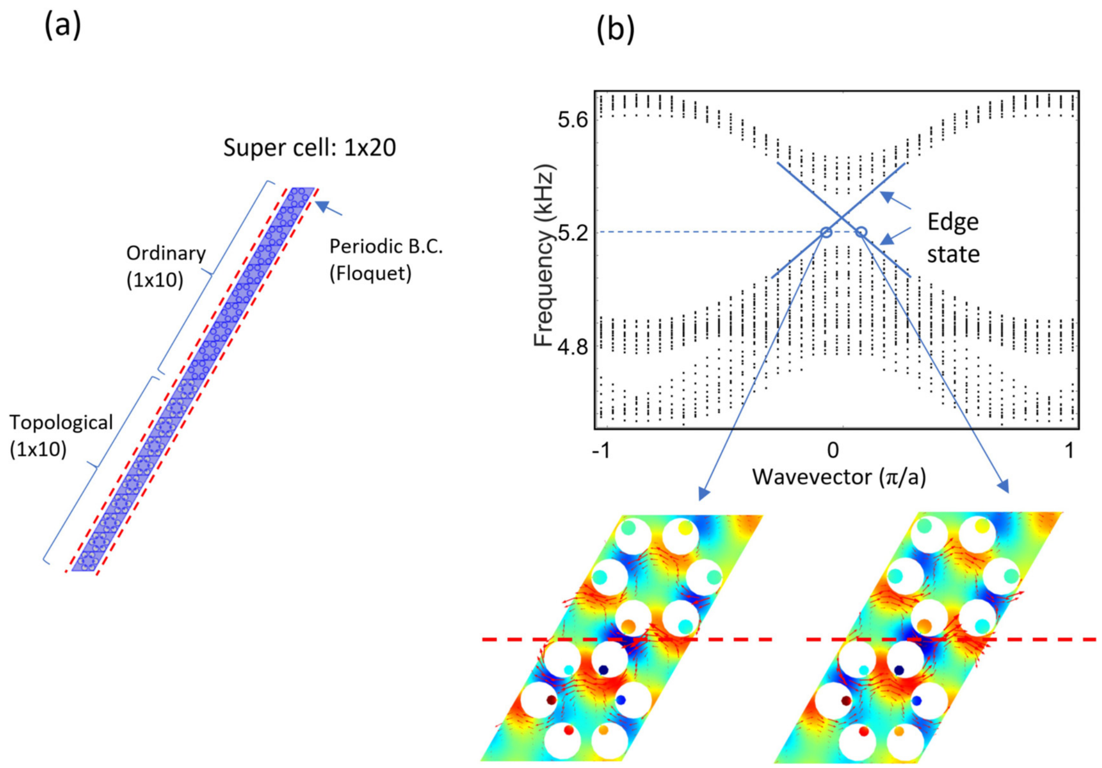

FIG. 6. (a) Supercell (1 × 20) for the topological edge state, composed of ordinary (1 × 10) and topological (1 × 10) unit cells. (b) Band structure of the supercell. In the bottom panel, the pressure fields around the edge are plotted at wave vectors of $\pm 0.075\pi/a$. The red arrows indicate the acoustic intensity vectors.

topological phases, since its structure contains narrow air slits capable of dissipating acoustic energy, which is similar to acoustic absorbers made of Helmholtz resonators [40,42]. Without end correction, viscous and thermal losses occurring in the slit (h) are considered by using effective parameters given as [42]

$$\rho_s = \rho_0\left[1 - \frac{\tanh\left(\frac{h}{2}G_\rho\right)}{\frac{h}{2}G_\rho}\right]^{-1}, \tag{4}$$

$$\kappa_s = \kappa_0\left[1 + (\gamma - 1)\frac{\tanh\left(\frac{h}{2}G_\kappa\right)}{\frac{h}{2}G_\kappa}\right]^{-1}, \tag{5}$$

where ρ_0 is the density and κ_0 is the bulk modulus, $G_\rho = \sqrt{i\omega\rho_0/\eta}$ and $G_\kappa = \sqrt{i\omega\mathrm{Pr}\rho_0/\eta}$, with γ the specific-heat ratio of air, η the dynamic viscosity, and Pr the Prandtl number ($\mathrm{Pr} = \frac{\eta}{\rho_0\alpha}$ with α the thermal diffusivity). As shown in the schematics of Fig. 7(a), these effective parameters are used only for the lossy slits, resulting in the complex speed of sound within the lossy slits ($c = \sqrt{\kappa_s/\rho_s}$) for the wave equation (see Appendix A). Equations (4) and (5) are valid for plane-wave propagation inside the slits (the slit width h is much smaller than the wavelength). The effective parameters take into account viscous and thermal losses, as they are expressed by the dynamic viscosity (η) and thermal diffusivity (α).

To demonstrate robust sound propagation, we consider lossy and lossless cases by using interfaces with two sharp corners, as shown in Fig. 7(a). The lossy case uses the effective parameters (i.e., ρ_s and κ_s) for the slits and the intrinsic properties (ρ_0 and κ_0) for the rest of the fluid regions. The top domain is the ordinary phase, whereas the bottom domain has a topological phase. We consider a source of plane acoustic waves (5200 Hz) on the left side, which is placed on the boundary (the source length of $3a$). In Fig. 7(a), we observe backscattering-free propagation regardless of the loss. Figure 7(b) shows absolute pressure amplitudes along the right boundary [output in Fig. 7(a)] for the lossless, small loss, and high loss cases. The small loss corresponds to the intrinsic loss in the slit [its actual width h_0 is used for Eqs. (4) and (5)], while the high loss uses the effective parameters obtained using a smaller $h = 0.5h_0$ for Eqs. (4) and (5). The pressure amplitudes are normalized to the peak value for the lossless case. Note that the acoustic amplitude along the right boundary (output ports) is considerably reduced for the small (red line) and high (blue line) losses. The acoustic pressure is confined along the interface between the two domains (i.e., the width at half maximum $<6\lambda_0$), although it extends near the top and bottom boundaries. The confinement can be enhanced by employing ordinary and topological domains with larger bulk band gaps [34]. The investigation on the lossy topological insulator indicates that topological insulators can demonstrate robust wave propagation despite their intrinsic losses. In addition, when the lossy resonators are replaced with energy conversion resonators, the lossy topological insulator can be modified into an energy-harvesting topological insulator.

IV. CONCLUSIONS

We have demonstrated a topological phase transition using honeycomb phononic crystals consisting of C-shaped rods.

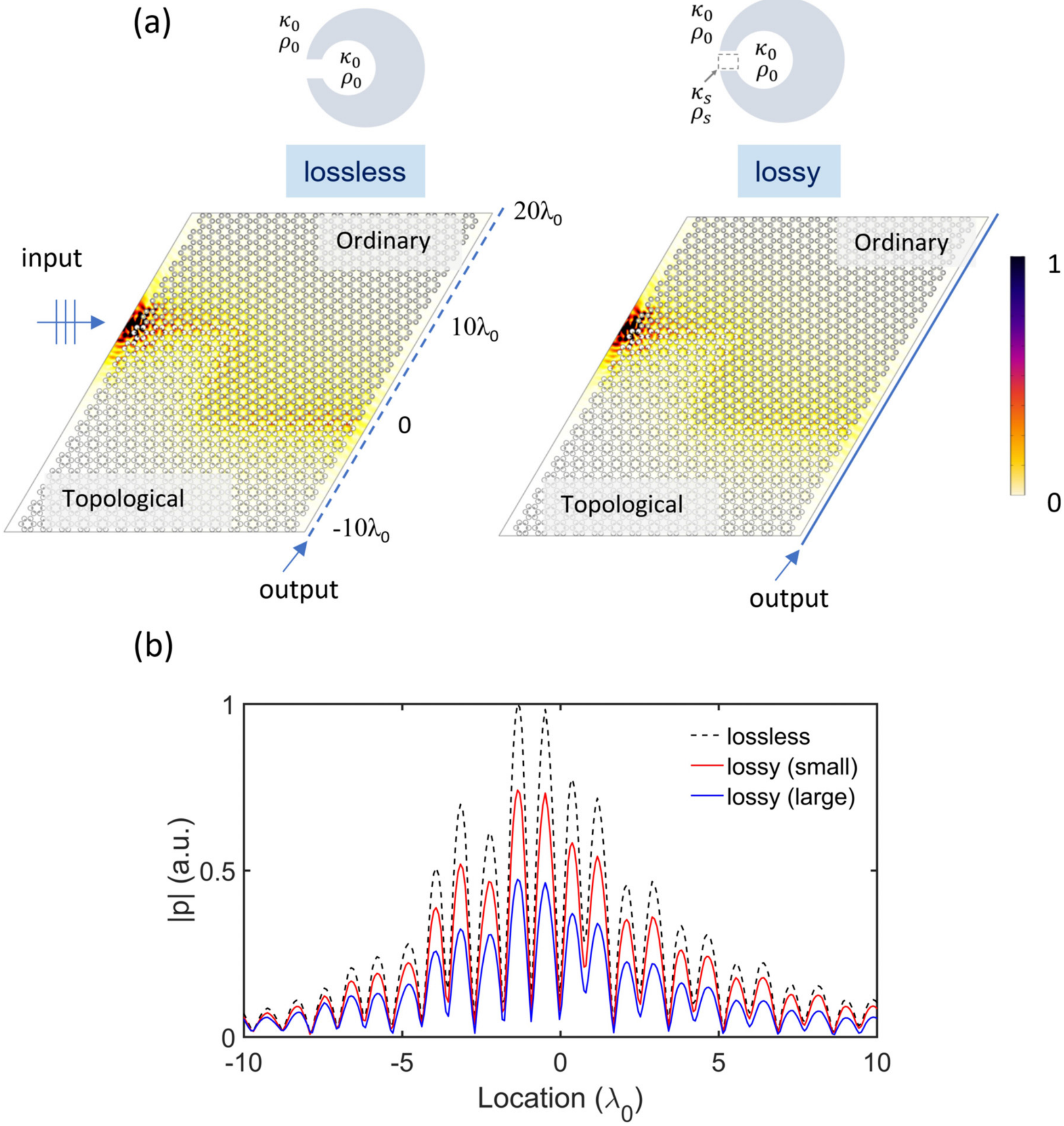

FIG. 7. (a) Effect of propagation loss on topological edge propagation. Backscattering-free zigzag edge propagation is demonstrated for the lossless (left) and lossy (right) cases. The illustration shows that the lossy case uses the effective parameters [ρ_s and κ_s from Eqs. (4) and (5)] for the slit region, while the lossless case uses the intrinsic parameters (ρ_0 and κ_0) for the entire fluid domain. Output ports along the right boundary, used for pressure magnitude, are highlighted by the blue dashed (lossless) and solid (lossy) lines. (b) Normalized pressure magnitude ($|p|$) at the output ports for lossless and lossy edge propagation at 5200 Hz. The pressure magnitude is normalized to the peak pressure of the lossless case.

Our phononic crystals have allowed us to investigate the interaction between Bragg scattering and local resonance, and each can be controlled independently in our phononic crystals. We have shown that the Bragg scattering induced gapless bands experience topological phase transitions due to local resonance, and that the band-gap size can be controlled by the resonance frequency relative to the Dirac cone frequency. Moreover, we have demonstrated a lossy topological insulator by adding loss in the resonant elements. In this lossy topological insulator, backscattering-free edge wave propagation is found to be preserved.

Our approach based on the interplay between Bragg scattering and local resonance can increase the degree of freedom for control of topological phases. An experimental verification of our findings is feasible by using 3D-printed C-shaped rods with the experimental setup found in Ref. [7], as long as the fabricated C-shaped rods have sufficient structural rigidity. In addition, our scatterers using local resonance can benefit from electrically tunable resonators for active topological insulators without needing any mechanical moving parts. Our results provide an understanding of the interaction between the scattering mechanisms and possibilities

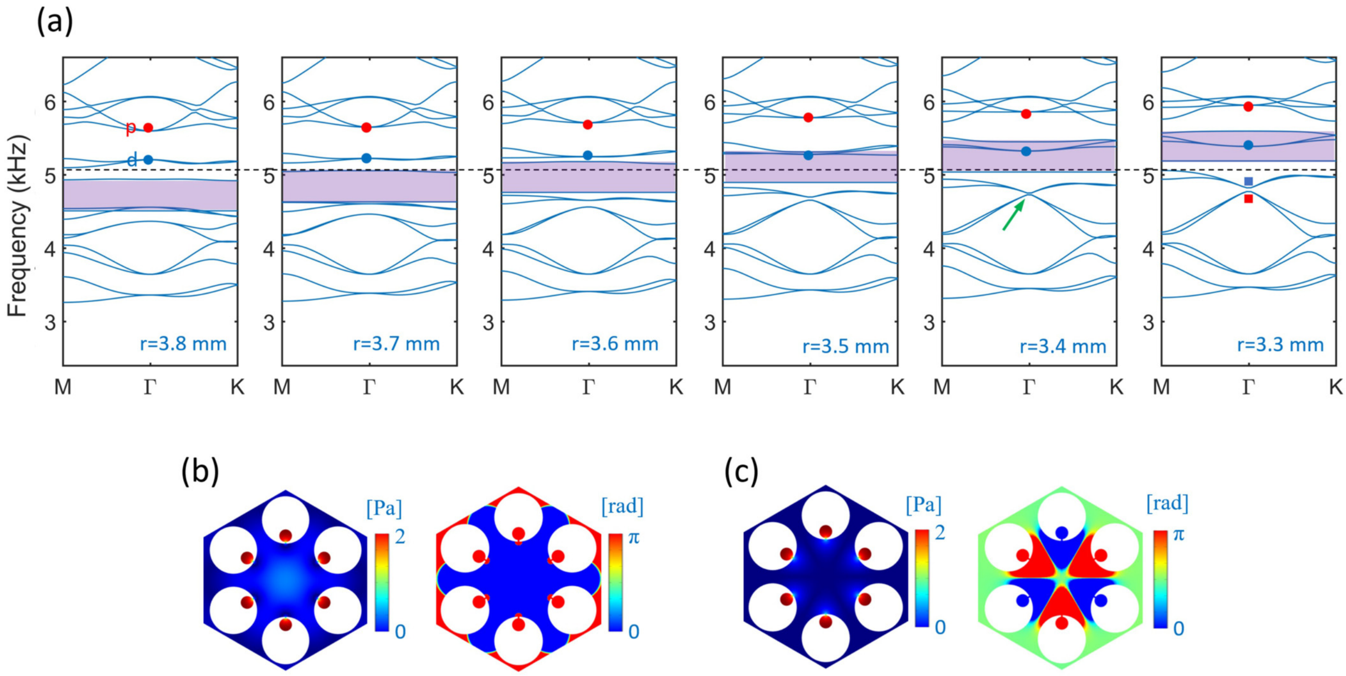

FIG. 8. (a) Band structures of the crystals ($\varphi = 180^\circ$) for resonance frequencies close to the Dirac cone frequency (5100 Hz). To control the resonance frequency, the radius (r) of the cavity is varied from $r = 3.8$ to 3.3 mm. The purple shade indicates two flat (upper and lower) horizontal bands related to the local resonance, while the dashed line indicates the Dirac cone frequency. The frequency of the lower flat band corresponds to the resonance frequency. The dipolar (quadrupolar) bands are highlighted by p with red circle symbols (d with blue circle symbols). For $r = 3.4$ mm, the green arrow indicates the double Dirac cone. (b, c) Acoustic intensity fields and phase plots for the lower flat bands (b) and upper flat bands (c) at $r = 3.8$ mm.

for designing fast-tunable or energy-harvesting acoustic topological insulators.

APPENDIX A: SIMULATION

All simulations are conducted using a commercial finite-element method solver, COMSOL Multiphysics 5.3 (pressure acoustic module). The solver numerically solves the wave equation in the two-dimensional (x and y coordinates) fluid domain, given by

$$\frac{\partial^2 p}{\partial x^2} + \frac{\partial^2 p}{\partial y^2} + \left(\frac{\omega}{c}\right)^2 p = 0, \tag{A1}$$

where p is the pressure, ω is the frequency, and c is the speed of sound ($c = \sqrt{\kappa/\rho}$ with κ and ρ being the bulk modulus and density). For losses in the narrow slits, the speed of sound used for the wave equation is modified by using the effective parameters [Eqs. (4) and (5)]. By assuming a large acoustic impedance mismatch between the background fluid and rigid scatterers, sound hard boundary conditions (i.e., Neumann condition) are applied to the fluid/solid interface, which are given by

$$\boldsymbol{n} \cdot \boldsymbol{\nabla} p = 0, \tag{A2}$$

where $\boldsymbol{n}$ is the normal vector to the boundary, $\boldsymbol{\nabla}$ is the vector differential operator (i.e., $\boldsymbol{\nabla} = \frac{\partial}{\partial x}\mathbf{i} + \frac{\partial}{\partial y}\mathbf{j}$ with $\mathbf{i}$ and $\mathbf{j}$ being the unit vectors in the x and y coordinates, respectively), and the dot symbol denotes the dot product of the two vectors. To calculate the bulk (edge) band structures, Floquet periodic boundary conditions are applied to periodic surfaces of the unit cell (supercell), which are given by

$$p_{\mathrm{dst}} = p_{\mathrm{src}} e^{i\boldsymbol{k}_F \cdot (\boldsymbol{r}_{\mathrm{dst}} - \boldsymbol{r}_{\mathrm{src}})} \tag{A3}$$

and

$$\boldsymbol{n}_{\mathrm{dst}} \cdot \boldsymbol{\nabla} p_{\mathrm{dst}} = \boldsymbol{n}_{\mathrm{src}} \cdot \boldsymbol{\nabla} p_{\mathrm{src}} e^{i\boldsymbol{k}_F \cdot (\boldsymbol{r}_{\mathrm{dst}} - \boldsymbol{r}_{\mathrm{src}})}, \tag{A4}$$

where the subscripts (dst and src) denote the destination boundary and source boundary, respectively, $\boldsymbol{k}_F$ is the k vector for Floquet periodicity, and $\boldsymbol{r}$ is the position vector. For phononic crystals, continuity boundary conditions, i.e., Eqs. (A3) and (A4) with $\boldsymbol{k}_F = 0$, are used for the top and bottom boundaries, and radiation boundary conditions are imposed on the left and right, which are given by

$$\boldsymbol{n} \cdot \boldsymbol{\nabla} p - i\frac{\omega}{c} p = Q_i, \tag{A5}$$

where Q_i is the source term. Here, the source term is zero except for a boundary for incident plane waves. The incident plane waves, the propagation direction of which is parallel to the interface between the ordinary and topological regions, are used for the input on the left boundary. In this case, Q_i is given by

$$Q_i = \boldsymbol{n} \cdot \boldsymbol{\nabla} p_i - i\frac{\omega}{c} p_i, \tag{A6}$$

where p_i is the incident pressure wave expressed by $p_i = p_0 e^{i\frac{\omega}{c}(\boldsymbol{r}\cdot\mathbf{e_k})}$ with p_0 the pressure amplitude and $\mathbf{e_k}$ the normalized wave direction vector. Here, the length of the excitation along the left boundary is three times the lattice constant (a).

The material properties of air are given by the density ($\rho_0 = 1.2\ \mathrm{kg/m^3}$) and the speed of sound ($c = 343\ \mathrm{m/s}$). For the lossy phononic crystals, the effective parameters [Eqs. (4) and (5)] are obtained by using additional air properties, which are given for room temperature (300 K) by the Prandtl number (Pr $= 0.707$), dynamic viscosity ($\mu = 1.85 \times 10^{-5}$Pa s), specific-heat ratio ($\gamma = 1.4$), and bulk modulus ($\kappa_0 = \gamma P_0$ for the ambient pressure $P_0 = 101.325$ kPa).

APPENDIX B: BAND STRUCTURE FOR $f_r = f_D$

Figure 8(a) shows the band structures for different radii (r). For comparison, bands with two twofold degenerate modes (p type and d type) are indicated by p and d, and two horizontal bands associated with local resonance are shaded in purple. These two horizontal bands are verified with strong pressure field inside the cavities, as seen in Figs. 8(b) and 8(c). We find that the lower-frequency horizontal band corresponds to the resonance frequency. By varying r, the resonance frequency (lower-frequency horizontal band) approaches the Dirac cone frequency (dashed line). For $r = 3.4$ mm, the resonance frequency meets the Dirac cone frequency. In this case, the upper-frequency horizontal band is placed within the band gap of the p-type and d-type bands. Note that the double Dirac cone occurs at a frequency lower than 5100 Hz (marked with a green arrow). In addition, the band gaps at M and K are smaller than the one at Γ, indicating that the resonance frequency can be placed as close to the Dirac cone frequency as possible, unless the bands related to local resonance interfere with the p-type and d-type bands.

APPENDIX C: CALCULATION OF THE SCATTERING CROSS SECTION

The scattering cross section of a scatterer in the 2D domain is given by the ratio of the scattered power (W/m) to the incident power ($\mathrm{W/m^2}$):

$$\sigma_{\mathrm{sc}}[m] = \frac{\int_s \frac{|p_{\mathrm{sc}}|^2}{2\rho c} ds}{\frac{|p_i|^2}{2\rho c}}, \tag{C1}$$

where p_{sc} is the scattered pressure and p_i is the incident pressure, i.e., Eq. (A6). The scattered pressure field is calculated numerically (COMSOL) or analytically [Eqs. (2) and (3)]. Then, the scattered power (W/m) is calculated by the integral taken over a circular line (s) of a radius (r_0) surrounding the scatterer. For the numerical calculation for the resonant configuration, the integration for the scatterer power is taken over a semicircle, as the resonant cavity is embedded in a semi-infinite reflector.

[1] L. Fu and C. L. Kane, Phys. Rev. Lett. **100**, 096407 (2008).
[2] H. Zhang, C.-X. Liu, X.-L. Qi, X. Dai, Z. Fang, and S.-C. Zhang, Nat. Phys. **5**, 438 (2009).
[3] Y. L. Chen, J. G. Analytis, J.-H. Chu, Z. K. Liu, S.-K. Mo, X. L. Qi, H. J. Zhang, D. H. Lu, X. Dai, Z. Fang, S. C. Zhang, I. R. Fisher, Z. Hussain, and Z.-X. Shen, Science **325**, 178 (2009).
[4] R. Fleury, A. B. Khanikaev, and A. Alù, Nat. Commun. **7**, 11744 (2016).
[5] Z. Yang, F. Gao, X. Shi, X. Lin, Z. Gao, Y. Chong, and B. Zhang, Phys. Rev. Lett. **114**, 114301 (2015).
[6] Z. Zhang, Q. Wei, Y. Cheng, T. Zhang, D. Wu, and X. Liu, Phys. Rev. Lett. **118**, 084303 (2017).
[7] C. He, X. Ni, H. Ge, X.-C. Sun, Y.-B. Chen, M.-H. Lu, X.-P. Liu, and Y.-F. Chen, Nat. Phys. **12**, 1124 (2016).
[8] P. Wang, L. Lu, and K. Bertoldi, Phys. Rev. Lett. **115**, 104302 (2015).
[9] J. Mei, Z. Chen, and Y. Wu, Sci. Rep. **6**, 32752 (2016).
[10] S.-Y. Yu, C. He, Z. Wang, F.-K. Liu, X.-C. Sun, Z. Li, H.-Z. Lu, M.-H. Lu, X.-P. Liu, and Y.-F. Chen, Nat. Commun. **9**, 3072 (2018).
[11] Y. Guo, T. Dekorsy, and M. Hettich, Sci. Rep. **7**, 18043 (2017).
[12] X. Wen, C. Qiu, J. Lu, H. He, M. Ke, and Z. Liu, J. Appl. Phys. **123**, 091703 (2018).
[13] A. Foehr, O. R. Bilal, S. D. Huber, and C. Daraio, Phys. Rev. Lett. **120**, 205501 (2018).
[14] C. Brendel, V. Peano, O. Painter, and F. Marquardt, Phys. Rev. B **97**, 020102(R) (2018).
[15] J. Chen, H. Huang, S. Huo, Z. Tan, X. Xie, J. Cheng, and G.-L. Huang, Phys. Rev. B **98**, 014302 (2018).
[16] H. Zhu, T.-W. Liu, and F. Semperlotti, Phys. Rev. B **97**, 174301 (2018).
[17] Y. Jin, D. Torrent, and B. Djafari-Rouhani, Phys. Rev. B **98**, 054307 (2018).
[18] D. Jia, H.-X. Sun, J.-P. Xia, S.-Q. Yuan, X.-J. Liu, and C. Zhang, New J. Phys. **20**, 093027 (2018).
[19] M. Miniaci, R. K. Pal, B. Morvan, and M. Ruzzene, Phys. Rev. X **8**, 031074 (2018).
[20] M. Serra-Garcia, V. Peri, R. Süsstrunk, O. R. Bilal, T. Larsen, L. G. Villanueva, and S. D. Huber, Nature (London) **555**, 342 (2018).
[21] F. Li, X. Huang, J. Lu, J. Ma, and Z. Liu, Nat. Phys. **14**, 30 (2018).
[22] W. Zhu, X. Fang, D. Li, Y. Sun, Y. Li, Y. Jing, and H. Chen, Phys. Rev. Lett. **121**, 124501 (2018).
[23] D. Zhao, M. Xiao, C. W. Ling, C. T. Chan, and K. H. Fung, Phys. Rev. B **98**, 014110 (2018).
[24] Z. Zhang, Y. Tian, Y. Wang, S. Gao, Y. Cheng, X. Liu, and J. Christensen, Adv. Mat. **30**, 1803229 (2018).
[25] J.-P. Xia, D. Jia, H.-X. Sun, S.-Q. Yuan, Y. Ge, Q.-R. Si, and X.-J. Liu, Adv. Mat. **30**, 1805002 (2018).
[26] J. Lu, C. Qiu, W. Deng, X. Huang, F. Li, F. Zhang, S. Chen, and Z. Liu, Phys. Rev. Lett. **120**, 116802 (2018).
[27] S.-Y. Huo, J.-J. Chen, H.-B. Huang, and G.-L. Huang, Sci. Rep. **7**, 10335 (2017).
[28] Z. Zhang, Y. Tian, Y. Cheng, Q. Wei, X. Liu, and J. Christensen, Phys. Rev. Appl. **9**, 034032 (2018).
[29] Z.-G. Geng, Y.-G. Peng, Y.-X. Shen, D.-G. Zhao, and X.-F. Zhu, Appl. Phys. Lett. **113**, 033503 (2018).

[30] S. Li, D. Zhao, H. Niu, X. Zhu, and J. Zang, Nat. Commun. **9**, 1370 (2018).

[31] T.-W. Liu and F. Semperlotti, Phys. Rev. Appl. **9**, 014001 (2018).

[32] J. Cha, K. W. Kim, and C. Daraio, Nature (London) **564**, 229 (2018).

[33] R. Chaunsali, C.-W. Chen, and J. Yang, Phys. Rev. B **97**, 054307 (2018).

[34] S. Yves, R. Fleury, F. Lemoult, M. Fink, and G. Lerosey, New J. Phys. **19**, 075003 (2017).

[35] R. Chaunsali, C.-W. Chen, and J. Yang, New J. Phys. **20**, 113036 (2018).

[36] C. Yilmaz, G. M. Hulbert, and N. Kikuchi, Phys. Rev. B **76**, 054309 (2007).

[37] M. Fruchart and V. Vitelli, Nature (London) **555**, 318 (2018).

[38] L.-H. Wu and X. Hu, Phys. Rev. Lett. **114**, 223901 (2015).

[39] J. J. Faran, Jr., J. Acoust. Soc. Am. **23**, 405 (1951).

[40] C. Lagarrigue, J. P. Groby, V. Tournat, and O. Dazel, J. Acoust. Soc. Am. **134**, 4670 (2013).

[41] Z. Gong, Y. Ashida, K. Kawabata, K. Takasan, S. Higashikawa, and M. Ueda, Phys. Rev. X **8**, 031079 (2018).

[42] N. Jiménez, W. Huang, V. Romero-García, V. Pagneux, and J.-P. Groby, Appl. Phys. Lett. **109**, 121902 (2016).